JOURNAL OF GEOPHYSICAL RESEARCH, VOL. 89, NO. C3, PAGES 3573–3580, MAY 20, 1984

Spectral Albedos of Sea Ice and Incident Solar Irradiance in the Southern Beaufort Sea

THOMAS C. GRENFELL

Department of Atmospheric Sciences, University of Washington

DONALD K. PEROVICH

Geophysics Program, University of Washington

Spectral albedos and incident spectral irradiances have been measured over the wavelength range 400 to 2400 nm on the sea ice near the Naval Arctic Research Laboratory (NARL) at Pt. Barrow, Alaska. The observation interval extended from mid-May, when the ice was still relatively cold, until mid-June, when summer melting was fully established. The temporal dependence of albedo for the available surface types was obtained over this time interval showing a general decrease from snow and snow-covered ice to blue ice and melt ponds. Data were also obtained for glacier ice on the Athabasca glacier, for melting lake ice, and for certain other nonice surfaces in the vicinity of NARL. Snow and ice albedos are characteristically highest at visible wavelengths, decreasing strongly in the infrared because of the increase in absorption by ice and water. Local maxima in the spectra correspond to minima in the ice and water absorption. Variations in albedo are due primarily to differences in the vapor bubble density, crystal structure, and free water content of the upper layers of the ice. Incident spectral shortwave radiation was measured as a function of cloudiness, and the optical thickness of arctic clouds is significantly less than the thickest clouds at lower latitudes. The decrease of the infrared component relatiave to the visible portion of the irradiance with increasing cloud cover is determined. This can give rise to an increase in wavelength-integrated albedos of as much as 15%. Using the present data, a graphical method is outlined by which visible near-infrared satellite imagery can be used to distinguish among melt ponds, open leads, and other spring and summer sea ice surface types.

1. INTRODUCTION

The interaction of shortwave radiation with sea ice is of primary importance in the local heat and mass balance of the ice cover, which in turn influences large-scale ice dynamics and polar climatology. In addition, considerable effort has been devoted to mapping the earth's surface via narrow-band visible and near-infrared imagery from space, and a number of satellite sensor packages that image the polar regions are now in operation or planned for the near future. These remote sensing techniques offer the possibility of investigating both ice concentration and surface type distribution over substantial portions of the Arctic Basin for more than half the year. Spectral albedos of the prevalent surface types are needed in this effort, especially if the ground resolution of the imagery is not high enough to resolve the fine surface details. It is important to take into account that the optical properties of the ice depend both on ice type and season, and large changes can occur rapidly over the course of the summer melt season. This has been described in detail by *Grenfell and Maykut* [1977].

Wavelength-integrated albedos and incident irradiance values have been obtained in the Arctic on many occasions [for example, *Chernigovskii*, 1963; *Langleben*, 1969, 1971; *Hanson*, 1961] but are of limited usefulness for the purposes described above. In particular, because the optical properties of the ice are dependent on wavelength [*Grenfell and Maykut*, 1977], a quantitative determination of solar heat input to the ice requires a detailed knowledge of the spectral albedo and the wavelength distribution of the incident radiation field. Grenfell and Maykut give wavelength-dependent values for the optical properties of a variety of ice types, but their data cover the spectrum only from 400 to 1000 nm, and the spectral resolution of their albedos is limited at longer wavelengths. They stress the importance of extending the albedo measurements to longer wavelengths, primarily because a significant fraction of the incident solar radiation lies in the infrared between 1000 and 3000 nm.

Incident solar spectra for the clearest skies and a very dry atmosphere have been reported by *Gast* [1960] for air masses as large as 5. These results are of high quality but are probably not appropriate to the summertime Arctic because the presence of melt ponds and open leads results in a very high moisture content and a nearly continuous cloud layer. Spectral data for overcast conditions are extremely scarce. Some very low resolution incident irradiances were presented by *Sauberer and Dirmhirn* [1958], which made it possible to show the importance of clouds in the radiative energy balance of the ice [*Grenfell*, 1979] but which left considerable uncertainty in the results; however, no high-resolution results have been reported for the polar regions.

2. FIELD PROGRAM

A series of observations to investigate surface albedos and incoming shortwave radiation over sea ice was carried out from May 18 through June 17, 1979, near the Naval Arctic Research Laboratory, at Point Barrow, Alaska. A visible and infrared scanning photometer, described below, was used to measure the incident and reflected spectral irradiances over a series of sites located on the sea ice between 1 and 3 km from shore. The direction from the laboratory for all sea ice sites was perpendicular to the prevailing winds to minimize the surface contamination by locally produced aerosols. The sites included shorefast ice, first- and second-year floes, and a highly deformed rubble zone. The time period was chosen to

Copyright 1984 by the American Geophysical Union.

Paper number 4C0130.
0148-0227/84/004C-0130$05.00

cover the transition from cold winter conditions, when the surface was predominantly snow covered, to the well-developed melt conditions typical of summer.

The photometer was contained in a 20-cm-diameter aluminum cylinder and was mounted on a tripod that supported the sensors about 1 m above the surface. Spectral dispersion was provided by a circular variable filter from 400 to 1400 nm and by a set of single-band interference filters from 1400 to 2400 nm, all of which were mounted on a disk that was rotated to select the desired wavelengths. The resolving power (wavelength divided by the bandwidth) ranged from 12 to 46, depending on wavelength. Three distinct imaging systems provided simultaneous readings in three different wavelength regions. From 400 to 1200 nm the photodetector was a silicon photodiode, and from 700 to 2400 nm, two lead sulfide detectors were used. Each optical train incorporated a turret-type "cosine collector" designed so that irradiance would be measured directly. For the visible and near infrared the turret was made of translucent plexiglas, while teflon was used from 1400 to 2400 nm. Further details of the instrument have been reported by *Grenfell* [1981].

Shadowing by the photometer was calculated numerically from the instrument geometry for a diffuse incident radiation field. It was also checked empirically by suspending the photometer at various heights between 0.5 and 4 m over a uniform horizontal surface and observing the variation in reflected irradiance. In both cases a shadowing correction of 1% was found to be appropriate for a 1-m observation elevation and has been applied to all our measured albedos.

To avoid uncertainties in wavelength registration, the photometer's filter wheel was stepped to a given wavelength and up- and down-looking observations were made. The instrument was then stepped to a new wavelength and the process repeated. A full set of observations at a single site was completed in about 30 min. Simultaneous measurements of total incident shortwave irradiance were taken with a calibrated Kipp and Zonen solarimeter. This made it possible to obtain albedo readings when the incident radiation field was not varying appreciably so that, even though variations occurred over the course of the run, they did not introduce significant error into the albedo results.

Incident spectral irradiances were also measured for a wide range of cloud conditions by recording continuous scans with a data logger. In this case a set of readings could be obtained in about 2 min. The solarimeter was again used to monitor down-welling irradiance so that the data could be recorded when the radiation field was steady.

Absolute calibration of the photometer was carried out by using a quartz halogen lamp obtained from Eppley Laboratory for which the emitted irradiance was traceable to a National Bureau of Standards standard source. Care was taken to operate the lamp according to specifications, including aligning the lamp with the optical axis of each channel. It was felt, though, that the uncertainty in absolute calibration is probably on the order of 10% because of the derived nature of the calibration. Instrument stability, however, was sufficiently good that individual scans could be repeated to better than 1% accuracy, and it showed no systematic drift.

The on-axis calibration was combined with the angular sensitivity of the detector to specify the instrument response. The true angular sensitivity over the operating wavelength range was determined by illuminating the instrument with a point source located 10 m away and varying the angle between the light and the optical axis of the photometer. The angular sensitivity of the detector was found to depart significantly from an ideal cosine response at infrared wavelengths. This is due to wavelength-dependent absorption by the opal plexiglas and teflon disks used in the "cosine collectors."

With this calibration it was possible to determine the incident irradiance on clear days. Both the total and the diffuse components of the incident radiation field were measured in order to obtain the direct solar component. The direct radiation was then corrected for the cosine error and recombined with the diffuse component. Spectral albedos, however, could not be determined accurately under clear skies because the upwelling radiation field was not completely diffuse, and moreover, they could not be determined with the instrumentation at hand. As a result the readings in such cases could not be adequately corrected to give true irradiances. To investigate this effect, several test sites were observed under both clear and cloudy skies. For cloudy conditions the wavelength dependence of the results was smooth and was found to be consistent with integrated albedos from the solarimeter data. Under clear conditions, however, the results were too high in the near infrared, and the measurements from the two channels for which different materials were used in the cosine collectors did not match in their region of overlap. Visual observations confirmed qualitatively that the upwelling radiance over snow on clear days was enhanced in the specular reflection direction. This anisotropy was apparently great enough to cause significant errors in the albedo. A general calibration for albedo was not feasible, since we were not equipped to measure the angular distribution of upwelling radiance. Albedo results are reported, therefore, only for overcast skies where the radiation field was diffuse. Under the prevalent weather conditions, this was not a significant restriction.

3. RESULTS

Spectral Albedos

An important aspect of the temporal behavior of the spectral albedos of sea ice (α_λ) is the general decrease that takes place with the onset of the melt season. As the snow decays the ice warms up to the melting point, and melt ponds form. For convenience we present three separate evolutionary sequences that represent the albedo trends observed and cover the complete range of ice surface types present in the study area. These should be thought of, in general, as a series of possible states through which an area of the surface can evolve rather than as unique evolutionary tracks expected for particular surface elements. In general it is difficult to predict how a particular surface element will evolve. Depending on local conditions, individual surface elements may switch from one evolutionary sequence to another. Although melt ponds tend to form in depressed areas, and drained white ice often occurs where drifting snow has inhibited melting, local cracking and drainage will often reverse these trends. For example, surface ablation can enlarge ponds at the expense of hummocks, but ponds can empty quite quickly if local drainage patterns change. Thus it is difficult to assign an albedo history for a particular surface element. For a complete characterization of regional sea ice albedos a statistical examination of surface-type distribution would be needed, but that is beyond the scope of the present study.

Figure 1 shows albedos for a 1.5-m-thick snow surface at the beginning of the experiment when the temperature was well below freezing (May 19) and again 7 days later (May 26)

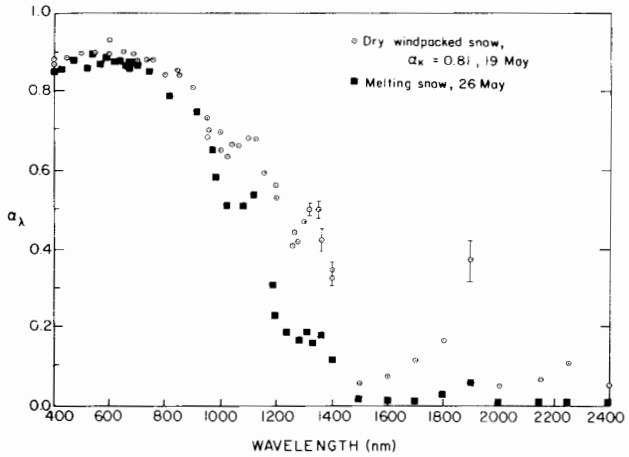

Fig. 1. Spectral albedos observed over snow: (dotted circles) dry wind-packed snow, $\rho_{surf} = 0.33$ mg/mm^3, $d_{grain} = 0.25$ mm; (filled squares) melting snow, $\rho_{surf} = 0.4$ mg/m^3, $d_{grain} = 0.5$ mm; α_k = integrated shortwave albedo.

after melting had set in. Physical changes in the snowpack during this period include an increase in the grain diameter from 0.25 mm to about 0.5 mm and an increase in snow density from 0.33 Mg/m^3 to about 0.4 Mg/m^3. The aging of the snow resulted in an albedo decrease at all wavelengths because the increase in grain size and rounding of the grains reduces the effective volume scattering. The largest changes occur in the infrared, where absorption by ice and water is very large and the upward scattered radiation is very sensitive to the scattering properties of individual grains at the surface.

As predicted by theoretical models [e.g., *Bohren and Barkstrom*, 1974], the decrease in snow albedos at visible wavelengths is quite small; however, the values are considerably lower than models indicate. Since the snow measurements were taken quite close to the laboratory, these low values are very likely caused by locally generated soot or other absorbing contaminants. The small change in visible albedo suggests that the contaminant level did not change between the two observation periods.

In Figures 1 through 7 the uncertainty in albedo is less than the size of the symbols, unless specifically indicated otherwise by error bars. The greatest uncertainty occurs when the incident irradiance is very low, particularly at 1400 nm and 1900 nm. For reference we also give concurrent results for wavelength-integrated shortwave albedos (α_K) measured with the Kipp and Zonen solarimeter. A comparison of these data with the spectral measurements will be given later in this section.

Temporal sequences for sea ice are shown in Figures 2 and 3. The former presents a series of cases for bare ice and melt ponds. The initial albedo for bare cold ice (May 22) shows a maximum at about 500 nm, with a nearly linear decrease out to 1400 nm. Blue ice occurs when the surface becomes saturated with meltwater, which fills in near-surface irregularities so that backscattering is reduced. This results in a reduction of the infrared albedo to the specular reflection limit, and the infrared albedo then remains constant for the ponds until they refreeze or drain completely. Figure 2 shows that for blue ice developing into melt ponds and for ponds that persist, the visible albedo continually decreases as the melt season progresses. This is probably a result of gradual decay of the underlying ice.

Figure 3 shows a sequence for snow-covered ice and drained white ice. The albedo is initially that of snow, since a cold snow layer of 5 to 10 cm is optically thick [*Grenfell and Maykut*, 1977]. As melting progresses the albedo decreases somewhat but remains considerably greater than for the previous sequence especially in the infrared. For the cases shown here, as the snow melts, the underlying ice has also warmed to the melting point, and brine or free water drains from the upper part of the ice, which is above the local freeboard level, giving rise to air inclusions that scatter efficiently. As a result the albedo of the surface decreases only slightly as the snow disappears, in contrast to areas where melt ponds form. This decrease appears to be fairly uniform across the spectrum, although the percentage change is actually largest in the infrared from 1500 to 2400 nm. As melting progresses the albedo of white ice does not decrease very much from 400 to about 1100 nm, presumably because, as the drained layer melts away, the ice rises to maintain hydrostatic balance so that the thickness of the drained layer remains nearly constant. At wavelengths

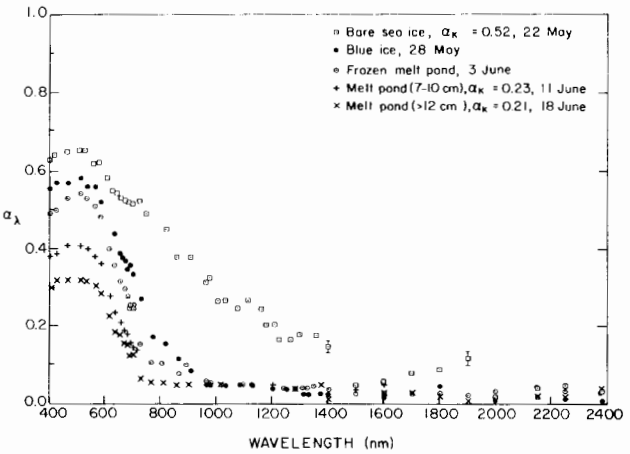

Fig. 2. Spectral albedos observed over bare ice and melt ponds. Integrated shortwave albedos and melt pond depths are indicated.

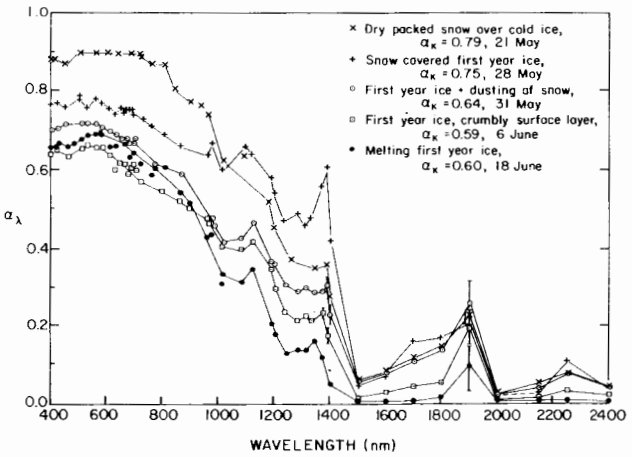

Fig. 3. Spectral albedos observed over snow-covered ice and drained white ice: (×) snow over cold ice, $z_{snow} = 8$ cm, $d_{grain} = 0.5$ mm, $\rho_{snow} = 0.34$ mg/m^3; (+) melting snow over first-year ice, $z_{snow} = 1$ cm, $d_{grain} = 0.5$ to 1 mm, $\rho_{snow} = 0.4$ mg/m^3; (dotted circles) first-year ice, 1-cm granular surface layer; (dotted squares) first-year ice, 1.5-cm crumbly granular surface layer (clusters of columns 2 to 3 mm in diameter and circular in cross section); (filled circles) melting first-year ice, 1.5-cm crumbly surface layer (clumps of grains 5 to 10 mm in size with small-scale irregularities of about 0.1 mm).

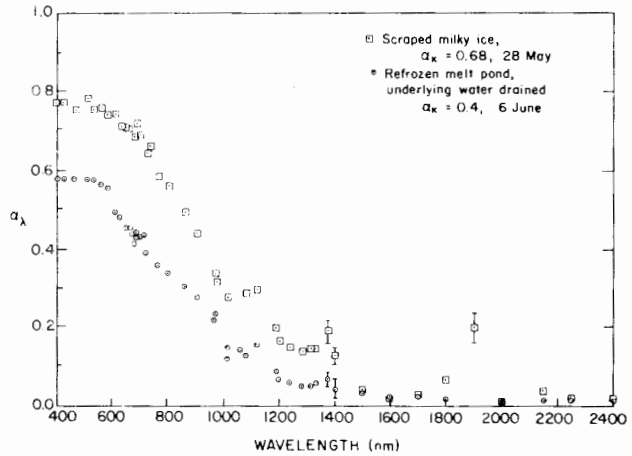

Fig. 4. Spectral albedos observed over (dotted squares) scraped milky ice with some subsurface melting and over (dotted circles) a refrozen drained melt pond.

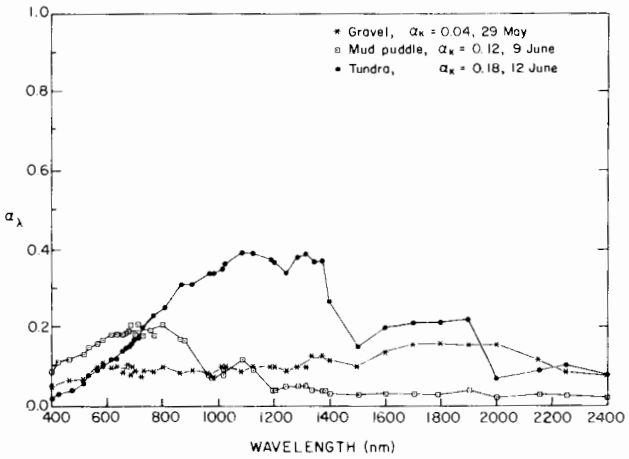

Fig. 6. Spectral albedos observed over beach gravel, tundra, and a well-stirred mud puddle (water depth approximately 30 cm).

beyond 1100 nm, though, the albedo decreases strongly as the crystal structure in the upper layers evolves toward rounded granules that backscatter less efficiently than the irregular crystals, which were present at first exposure of the surface. Note that the upper two curves cross at about 1000 nm and the lower two cross at about 900 nm. This may be due to vertical variations of the optical properties of the ice.

Spectral albedos were also obtained for a variety of other surfaces encountered in the vicinity of the laboratory that are of interest at polar latitudes. Figure 4 shows the results for sea ice with a very high bubble content, which caused it to appear milky, and for a melt pond that had frozen over and when the remaining water had drained away. For the milky ice, melting was beginning just below the surface, and later it formed a breakable crust. In this case, α_λ is higher at visible wavelengths than drained ice, and the decrease in α_λ with increasing wavelength is considerably stronger than for snow-covered ice or melting white ice. This is because most of the bubbles do not break the surface, so that surface scattering is minimal, and at longer wavelengths, absorption is dominant. The appearance and albedo of the drained melt pond are very similar to that of bare cold sea ice. While neither of these cases represents a major fraction of the ice cover, both occur often enough that they are of interest.

Figure 5 shows albedos of nearly freshwater ice in Imikpuk Lake. This case is unusual because the ice had a pronounced greenish cast to it, presumably because of the growth of algae in intercrystalline spaces below the water line. At the time the measurements were made, the ice was melting and had hydrostatically relaxed, resulting in a 13-cm-thick drained layer over most of the surface. In this regard it was similar to the sea ice; however, the crystal structure of the drained layer consisted of larger crystals and was more strongly etched out. Observations were made over a drained area and over a melt pond whose color was quite green. The greenish appearance is evident in the albedo curves, which show a significant depression between 400 and 550 nm compared with white ice and melt ponds in Figures 2 and 3. The albedo of the drained ice was lower than for the melting first-year ice (curve ●, Figure 3) by about 0.05 in the visible and 0.1 in the near-infrared wavelengths.

Albedos of other natural surface types were also measured and are shown in Figure 6. These surfaces include shore gravel (commonly encountered in a strip several hundred meters wide along much of the north slope and the barrier islands), a representative patch of tundra just after meltout, and a well-mixed mud puddle. The shore gravel has a low albedo that rises from 0.04 at 400 nm to about 0.08 at 500 nm and remains constant to about 1500 nm. A broad maximum of about 0.15

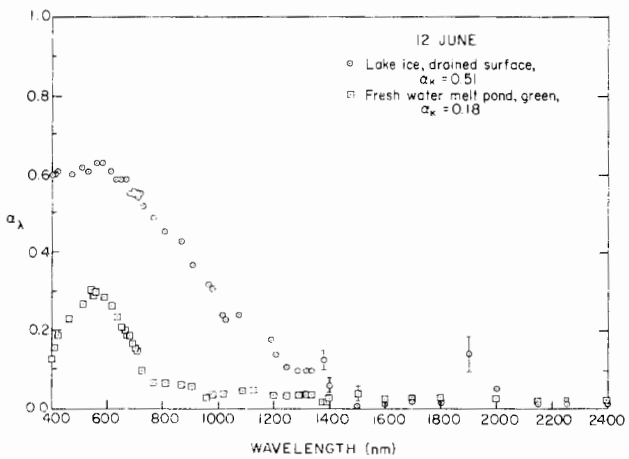

Fig. 5. Spectral albedos observed over lake ice: (dotted circles) drained white ice (drained layer thickness = 13 cm); (dotted squares) green melt pond (water depth = 7.5 cm).

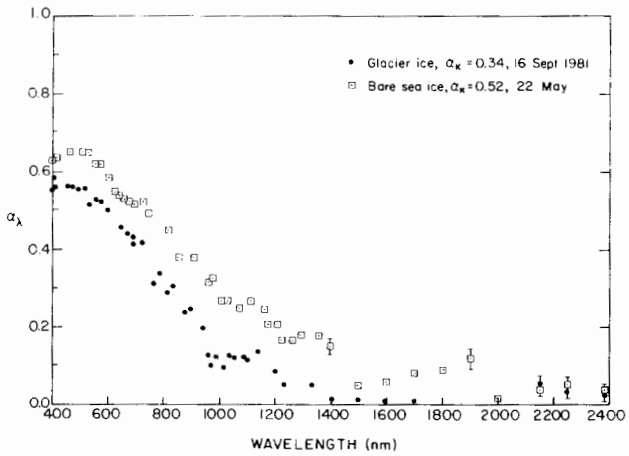

Fig. 7. Spectral albedo of glacier ice compared with bare sea ice (May 22).

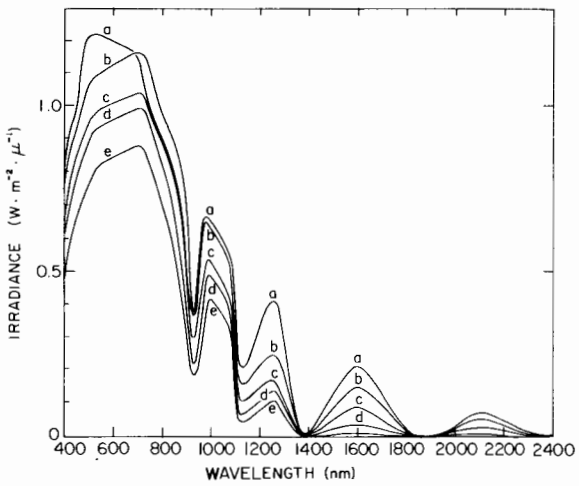

Fig. 8. Incident spectral irradiance versus cloud cover near local noon: (*a*) clear sky, dry clear atmosphere, air mass = 2, smoothed results from *Gast* [1960]; (*b*) sparse clouds and unobscured solar disk, June 9, solar zenith angle 49°; (*c*) overcast sky, solar disk visible, May 22; (*d*) overcast sky, solar disk barely visible, May 22; (*e*) heavy overcast, solar disk not visible, May 19. Corresponding integrated incident shortwave radiation is given in Table 2.

extends from 1700 to 2000 nm. Its visual appearance is grayish black and it consists of well-rounded stones, typically a few centimeters in diameter. The tundra and the stirred mud puddle albedos have a similar slope in the visible wavelengths, consistent with their brownish appearance; however, the tundra albedo is greater and continues to rise in the infrared to a maximum near 1300 nm. The mud puddle albedo decreases beyond 800 nm because of increasing absorption by the water.

A final case is shown in Figure 7, where the albedo of bare sea ice is compared with that of the Athabasca Glacier. The glacier ice data were taken in late summer 1981. The topmost few centimeters of ice were scraped off to remove much of the windblown dust that had collected there. The wavelength dependence appears to be about the same as for drained sea ice, although the values are about 0.05 lower. The glacier ice results are also quite similar to the freshwater lake ice shown in Figure 5. This is essentially the albedo for bubbly granular ice. Although some dust was probably still present, no samples were obtained for quantitative study.

Incident Spectral Irradiance

Figure 8 shows the variations observed in the incident spectrum over a snow surface versus cloud conditions ranging from clear skies to a thick continuous cloud cover. The figure caption gives a qualitative description of the local cloud conditions. Each case shown represents the average results for two to six individual scans. A more formal description of the cloud cover, kindly provided by the Pt. Barrow weather bureau office, is given in Table 1. To compare the solar energy in various wavelength bands, the curves were integrated by using a planimeter and the results compiled in Table 2. The table gives both the integrated irradiance for the particular band (including total shortwave) and the corresponding percentage of the total.

As is evident in Figure 8 the incident radiation decreases at all wavelengths with increasing cloud cover and thickness. The changes are strongest in the infrared because of the influence of the atmospheric water content, resulting in an increase in the ratio of visible-to-total irradiance. This is indicated quantitatively in Table 2, which shows that the percentage of radiation in the visible and near-infrared wavelengths increases from about 69% under clear conditions to more than 84% for full overcast. The percentage in all other bands decreases with increasing cloudiness as the water vapor bands increase in strength and absorption by liquid water in the clouds rises.

Also shown for comparison is the solar spectrum, observed for a very clear dry atmosphere by *Gast* [1960], for an incidence angle of 60° (an air mass of 2). This curve has been smoothed to match the spectral resolution of our instrument. It is greater than curve *b* at all wavelengths, except from about 700 to 900 nm. Because the lower troposphere over summer sea ice is, as a rule, saturated with water vapor, even on clear days, while curve *a* was obtained at high altitude for a very dry atmosphere, it is reasonable that curve *a* should be higher in the infrared than any of the present spectra, even though curve *b* is associated with a smaller air mass of 1.5. For this reason, though, we might expect that curve *b* would be greater than curve *a* between 400 and 900 nm, where the effects of water vapor are weak. Between 400 and 700 nm, the shape of the present spectra is more characteristic of an air mass of 3,

TABLE 1. Cloud Conditions at 23:15 GMT

Case and Date	Sky and Ceiling	Horizontal Visibility, km	Total Sky Cover	Lowest-Layer Coverage, Type, and Elevation	Second-Layer Coverage, Type, and Elevation
(*a*) 1960	Clear	not available	0/10		
(*b*) June 9	9000′ sct 20000′ sct	12	1/10	0/10	1/10 altocumulus 7000′
(*c*) May 22	800′ sct, est. 7000′ ovc	12	10/10	5/10 stratus 800′	5/10 altocumulus 7000′
(*d*) May 22	800′ sct, est. 7000′ ovc	12	10/10	5/10 stratus 800′	5/10 altocumulus 7000′
(*e*) May 19	M 1000′ ovc	12	10/10	10/10 stratus 1000′	not visible

Reported by the Point Barrow office of the National Weather Service on days when irradiance measurements were made.

TABLE 2. Incident Solar Irradiance in W/m^2 for Selected Wavelength Bands and Varying Degrees of Cloudiness Together With the Corresponding Relative Values

Case and Date	400–930 nm	930–1120 nm	1120–1390 nm	1390–1860 nm	1860–2400 nm	400–2400 nm,
(*a*) 1960	510/68.9%	105/14.2%	61/8.2%	49/6.6%	16/2.1%	741
(*b*) June 9	514/74.3%	93/13.5%	39/5.6%	34/4.9%	12/1.7%	692
(*c*) May 22	457/77.6%	77/13.1%	27/4.6%	22/3.7%	6/1.0%	589
(*d*) May 22	421/82.2%	65/12.7%	21/4.1%	5/1.0%	0/0	512
(*e*) May 19	364/84.8%	50/11.6%	15/3.6%	0/0	0/0	429

suggesting that Rayleigh scattering is stronger in the arctic atmosphere. This may arise because the results of *Gast* [1960] have presumably been reported for conditions of very low atmospheric opacity.

An interesting aspect of the present results is that the range of integrated irradiances from clear to heavy overcast is on the order of a factor of 2 to 3. This is also evident in the work of *Weaver* [1970] and *Herman* [1977]. At lower latitudes the range is a factor of 5 or more. We have observed cloud transmissivities of less than 20%, for example, during calibration of the solarimeters in Seattle. Thus, while clouds are usually present in the Arctic Basin, they tend to be thin so that their attenuation is generally weaker than at lower latitudes.

Integrated Albedos

As pointed out by *Grenfell and Maykut* [1977], variations in the solar spectrum with cloudiness imply accompanying changes in integrated albedos. Although direct observations would have been difficult to obtain because the surface characteristics were continually changing with the onset of melting, the incident spectral irradiances can be used to calculate what changes might be expected. One must assume that the spectral albedos themselves do not vary much with changes in cloudiness. Fortunately, the calculations of *Warren and Wiscombe* [1980] for snow, as well as unpublished calculations of our own for sea ice, suggest that this is a good approximation. Therefore, we present in Table 3 a set of integrated albedos determined from the formula

$$\alpha_j = \frac{\int_{400}^{2400} \alpha_\lambda F_j(\lambda)\, d\lambda}{\int_{400}^{2400} F_j(\lambda)\, d\lambda} \qquad (1)$$

where $F_j(\lambda)$ is the incident spectral irradiance for cloud state j. The resulting albedo variations are smaller than those predicted by Grenfell and Maykut because the reduction of the near infrared was not as strong as they had assumed. The calculations agree with the observed values for overcast conditions to within the tolerances of the observations. During the albedo measurements, we actually recorded values of integrated incident irradiance that were 20% lower than case (*e*) in Figure 8. Because these measurements took on the order of 30 min to complete, substantial fluctuations occurred in the radiation field, and reliable spectra could not be recovered. The data indicate, though, that the decrease in the relative contribution from the infrared continues for greater cloud thickness. This suggests that the albedo variation should be somewhat larger than we report in Table 3.

TABLE 3. The Effect of Cloudiness on Integrated Albedo

Surface Type	α_{cloudy}	α_{clear}	$\Delta\alpha$	α_{obs}(cloudy)
Snow	0.83	0.77	0.06	0.81 ± 0.04
Cold bare ice	0.49	0.43	0.06	0.52 ± 0.03
Melting white ice	0.58	0.53	0.05	0.59 ± 0.03
Blue ice	0.32	0.28	0.04	
Melt pond	0.23	0.21	0.02	0.23 ± 0.02

4. DISCUSSION

The wavelength dependence of the albedo of sea ice can be understood in terms of the rapid rise in volume absorption with wavelength [*Grenfell and Perovich*, 1981] together with substantial volume scattering caused by brine and vapor inclusions, which is nearly independent of wavelength. This is described in detail by a recent theoretical study [*Grenfell*, 1983] and is qualitatively the same as the explanation for snow [*Wiscombe and Warren*, 1980].

An important application for the albedo data is to interpret visible and near-infrared satellite images of the Arctic. For cases where surface features, such as melt ponds and narrow leads, cannot be resolved, results from the present study can be used to infer information about surface-type distribution by exploiting the color and contrast differences. We have selected for each of three specific satellite packages (LANDSAT C, LANDSAT D MSS, and Nimbus 7 CZSC) a combination of channels designed to distinguish white ice/snow, melt ponds, and open water under summer conditions. The intensity that would be observed in a given channel is estimated by multiplying the albedo by the incident irradiance for a clear sky. This involves the assumptions that the spectral dependence of the radiation scattered by the surface toward the satellite sensor can be represented by α_λ multiplied by the incident irradiance. To first order this can be justified by our visual observations, which indicate that the color and contrast of different surface types is nearly independent of zenith angle from 0° to more than 70°. Improving the accuracy of this technique would involve an extensive set of observations or a considerable amount of computation with a radiative transfer model, both of which are beyond the scope of the present work.

For each satellite package the intensity in the shortest-wavelength channel is compared with the intensity ratio of that channel to a near-infrared channel. The short-wavelength channel takes advantage of the high contrast between snow or ice and open water, and the intensity ratio provides a measure of the color. In order to avoid the necessity for absolute calibration of the satellite data the intensity is normalized by the brightness expected for snow. Atmospheric effects are assumed to have been removed. The discrimination provided by the

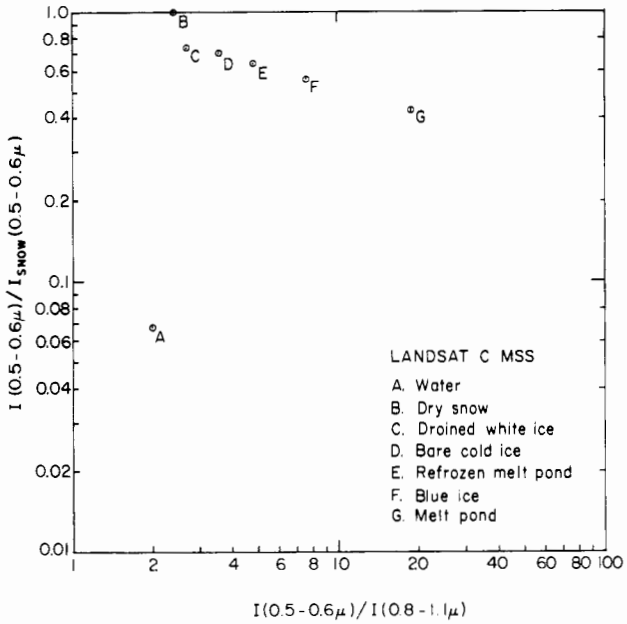

Fig. 9*a*.

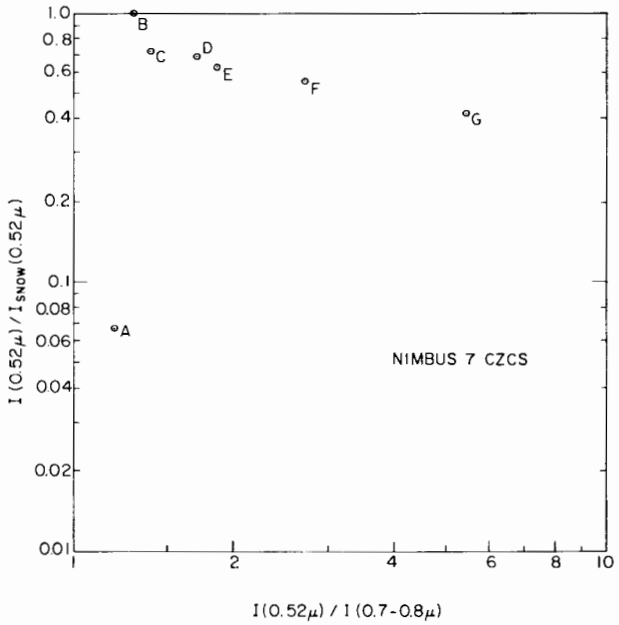

Fig. 9*c*

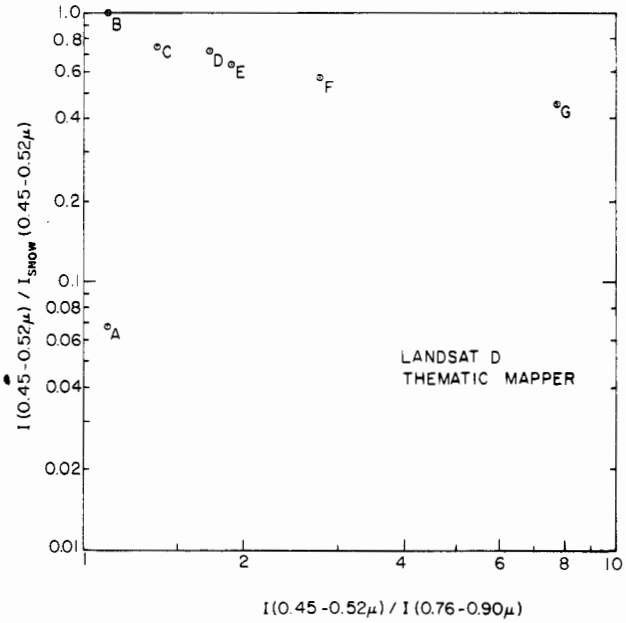

Fig. 9*b*.

Fig. 9. (*a*) Brightness versus color of spring/summer arctic ice surface types for LANDSAT C MSS. (*b*) Brightness versus color of spring/summer arctic ice surface types for LANDSAT C thematic mapper. (*c*) Brightness versus color of spring/summer arctic ice surface types for Nimbus 7 CZSC.

LANDSAT channels is slightly better than for the CZSC. All three, however, give a color range of an order of magnitude and should be equally useful in distinguishing summer surface types. The results are shown in Figure 9(*a*, *b*, *c*). Open water is strongly separated from all ice types, and the different ice surfaces are spread out along a color line from snow to melt ponds.

For an image element containing unresolved surface features, the observed location in this type of intensity-color diagram would indicate the percentage of area covered by the various ice types. Departures from the color line indicate the amount of open water, and the color would give information about the area covered by melt ponds. Generally, during high summer, the occurrence of blue ice is rare, and the snow cover is gone, so that essentially only two surface types are present. In this case the specification of the degree of ponding would be quite accurate. Although the cloud cover over the Arctic Basin is nearly complete during the summer, visible satellite imagery appears to show that up to 5% of the area is cloud free (R. T. Hall, personal communication, 1983). While this is not sufficient for a detailed survey of melt pond coverage, it would provide a basis for related studies. For example, information of this sort would be especially useful in conjunction with microwave imagery to improve estimates of summer ice concentration. If successful, it would be one of the few means capable of distinguishing melt ponds from leads with remote sensing techniques.

Acknowledgments. We are indebted to Steve Warren for helpful suggestions and a careful reading of the manuscript, and we would like to thank the Naval Arctic Research Lab for support and cooperation. This work was made possible by continuing support from the Office of Naval Research, Arctic Program under contract N00014-76-C-0234.

REFERENCES

Bohren, C. F., and B. R. Barkstrom, Theory of the optical properties of snow, *J. Geophys. Res.*, *79*(30), 4527–4535, 1974.

Chernigovskii, N. T., Radiatsionnyye svoystva ledyanogo pokrova tsentral'noy Arktiki (Radiation properties of the central arctic ice cover), Tr. Arkt. Antarkt. Nauch. Issled. Inst., *253*, 249–260, 1963.

Gast, P. R., Solar radiation, in *Handbook of Geophysics*, edited by C. F. Campen, pp. 16-14–16-32, Macmillan, New York, 1960.

Grenfell, T. C., The effects of ice thickness of the exchange of solar radiation over the polar oceans, *J. Glaciol.*, *22*(87), 305–320, 1979.

Grenfell, T. C., A visible and near-infrared scanning photometer for field measurements of spectral albedo and irradiance under polar conditions, *J. Glaciol.*, *27*(97), 476–481, 1981.

Grenfell, T. C., A theoretical model of the optical properties of sea ice in the visible and near infrared, *J. Geophys. Res.*, *88*(C11), 9723–9735, 1983.

Grenfell, T. C. and G. A. Maykut, The optical properties of ice and snow in the Arctic Basin, *J. Glaciol.*, *18*(80), 445–463, 1977.

Grenfell, T. C., and D. K. Perovich, Radiation absorption coefficients

of polycrystalline ice from 400 to 1400 nm, *J. Geophys. Res.*, *86*(C8), 7447–7450, 1981.

Hanson, K. J., The albedo of sea ice and ice islands in the Arctic Ocean Basin, *Arctic*, *14*(3), 188–196, 1961.

Herman, G. F., Solar radiation in summertime arctic stratus clouds, *J. Atmos. Sci.*, *34*, 1423–1432, 1977.

Langleben, M. P., Albedo and degree of puddling of a melting cover of sea ice, *J. Glaciol.*, *8*(54), 407–412, 1969.

Langleben, M. P., Albedo of melting sea ice in the southern Beaufort Sea, *J. Glaciol.*, *10*(58), 101–104, 1971.

Sauberer, F., and I. Dirmhirn, Das Strahlungsklima, in *Klimatographie von Oesterreich*, vol. 3, edited by F. Steinhauser, O. Eckel and F. Lauscher, pp. 13–102, Denkschrift der Gesamptakademie, Wien, 1958.

Warren, S. G., and W. J. Wiscombe, A model for the spectral albedo of snow, 2, Snow containing atmospheric aerosols, *J. Geophys. Res.*, *37*(12), 2734–2745, 1980.

Weaver, D., Radiation regime over arctic tundra and lake, *Sci. Rep. 6*, U.S. Office Nav. Res. Contract N00014-67-0103-007, Proj. 307-252, Dep. Atmos. Sci., Univ. Wash., Seattle, 1970.

Wiscombe, W. J., and S. G. Warren, A model for the spectral albedo of snow, 1, Pure snow, *J. Atmos. Sci.*, *37*(12), 2712–2733, 1980.

T. C. Grenfell, Department of Atmospheric Sciences AK-40, University of Washington, Seattle, WA 98195.

D. K. Perovich, Geophysics Program AK-50, University of Washington, Seattle, WA 98195.

(Received June 10, 1983;
revised January 16, 1984;
accepted January 17, 1984.)